

Phosphorus-doped Ni–Co sulfides connected by carbon nanotubes for flexible hybrid supercapacitor

Shengwang Su, Li Sun (✉), Feng Xie, Jialong Qian, Yihe Zhang (✉)

Engineering Research Center of Ministry of Education for Geological Carbon Storage and Low Carbon Utilization of Resources, Beijing Key Laboratory of Materials Utilization of Nonmetallic Minerals and Solid Wastes, National Laboratory of Mineral Materials, School of Materials Science and Technology, China University of Geosciences, Beijing 100083, China

© Higher Education Press 2023

Abstract As promising electrode materials for supercapacitors, nickel-cobalt bimetallic sulfides render the advantages of abundant redox reactions and inherently high conductivity. However, in general, unsatisfactory performance of low specific capacity, low rate capability, and fast capacity loss exist in Ni–Co sulfide electrodes. Herein, we rationally regulate phosphorus-doped nickel–cobalt sulfides (P-NCS) to enhance the electrochemical performance by gas–solid phosphorization. Moreover, carbon nanotubes (CNTs) as conductive additives are added to improve the cycle stability and conductivity and form the composite P-NCS/C/CNT. According to density functional theory, more electrons near the Fermi surface of P-NCS are demonstrated notionally than those of simple CoNi_2S_4 . Electrochemical results manifest that P-NCS/C/CNT exhibits superior electrochemical performance, e.g., high specific capacity ($932.0 \text{ C}\cdot\text{g}^{-1}$ at $1 \text{ A}\cdot\text{g}^{-1}$), remarkable rate capability (capacity retention ratio of 69.1% at $20 \text{ A}\cdot\text{g}^{-1}$), and lower charge transfer resistance. More importantly, the flexible hybrid asymmetric supercapacitor is assembled using P-NCS/C/CNT and activated carbon, which renders an energy density of $34.875 \text{ W}\cdot\text{h}\cdot\text{kg}^{-1}$ at a power density of $375 \text{ W}\cdot\text{kg}^{-1}$. These results show that as-prepared P-NCS/C/CNT demonstrates incredible possibility as a battery-type electrode for high-performance supercapacitors.

Keywords cobalt nickel sulfide, phosphorus-doping, hybrid supercapacitor, carbon nanotube, density functional theory

1 Introduction

Clean energy is bound to find vast development prospects

Received June 26, 2022; accepted September 10, 2022

E-mails: sunli@cugb.edu.cn (Sun L.), zyh@cugb.edu.cn (Zhang Y.)

under the trend of abandoning the reliance on fossil fuels and converting to new, environment-friendly energy. As a device to realize the storage of clean energy, the supercapacitor has always been a favorable competitor considering its advantages of safety, no memory effect, convenient maintaining, and reliability. It is also a mature portable energy storage device that has been widely used in daily life. Among the components of a supercapacitor system, the electrodes, especially the active materials, is a crucial component in determining whether a supercapacitor can obtain satisfactory performances, including high charge storage capacity, high energy, and power densities, excellent operating life, and fast charging/discharging rate [1–3].

In general, the classifications of supercapacitor electrode materials are proposed in terms of their energy storage mechanism, including the electrochemical double layer capacitive (EDLC) materials that rely on rapid ion adsorption and pseudocapacitive materials that exhibit fast surface faraday redox reactions [4]. Based on the material selection of its two electrodes, a supercapacitor mainly falls into three types, namely the electric double-layer capacitor that uses EDLC materials as both electrodes, the pseudocapacitor that uses pseudocapacitive materials for both electrodes, and the hybrid supercapacitor that uses pseudocapacitance material for the positive electrode and EDLC material for the negative electrode. Hybrid supercapacitors can combine the two primary energy storage mechanisms and constitutes an ideal energy storage mechanism [5]. In hybrid supercapacitors, the EDLC-based negative electrode mainly utilizes carbon materials, which give a highly stable but small charge storage capacity. Therefore, the positive electrode of pseudocapacitive materials contributes to enhancing the overall capacitive property.

Up till now, numerous work has been done on applying transition metals, oxides, and hydroxides in supercapacitor electrodes. New design concepts have been reported

to achieve better capacitive properties [6]. Numerous studies have proved that metal oxides and hydroxides can increase charge storage capacity and energy density compared to conventional carbonaceous materials. However, the main obstacle lies in their poor electrical conductivity, which causes intrinsic unfavorable kinetics of metal oxides and hydroxides and leads to their unsatisfactory rate performance [7,8]. In a contrast, metal phosphides and sulfides have a considerable intrinsic advantage as pseudocapacitive materials in supercapacitors because of their distinctive physicochemical properties. For instance, metal sulfides have the benefits of containing more redox-active sites and better specific capacities and energy densities [9–13]. Metal-rich phosphides have even higher electrical conductivity due to their relative metal richness [14–18]. It has also been proved that the combination of metal phosphides and sulfides can combine the advantages of both compounds and obtain enhanced cycle stability and rate performance compared to a single compound. By constructing phosphide–sulfide structures by doping P in sulfides or doping S in phosphides, extra active sites and additional voids can be created, which leads to promoting redox reactions and reduced strain [19–26]. Apart from forming phosphide–sulfide structures, new carbon materials can also be used to provide the basic structure and electrical conductivity for metal compounds, giving an additional contribution to performance enhancement [27–32].

Based on the above concepts, a facile method is designed in this work to fabricate a supercapacitor electrode material that features by ZIF-67 derived phosphorus-doped Ni–Co sulfides/carbon (P-NCS/C) complex embedded in carbon nanotube (CNT) basic structures and is also denoted P-NCS/C/CNT hereinafter. The P-NCS/C complex is realized by direct sulfuration of ZIF-67, plus a following vapor phosphorization reaction. The energy state and electron structures of CoNi_2S_4 before and after P-doping are theoretically studied to reveal the advantageous features of P-doped CoNi_2S_4 in electrode applications. Remarkable charge transfer properties and matter exchange efficiency are rendered by the P-NCS/C/CNT composite electrode by combining morphology advances from CNT-strengthened basic structure, ZIF-67 derived closer integration between carbon and Ni–Co compounds and combined advantage of Ni–Co sulfides and phosphides. A flexible hybrid supercapacitor is also assembled, possessing high energy/power density.

2 Experimental

2.1 Material synthesis

2.1.1 Preparation of ZIF-67@CNT

First, carboxy-CNTs (c-CNTs, $\geq 99.0\%$, XFNANO) and

10 mg of cetyltrimethylammonium bromide ($\geq 99.0\%$, Coolaber) were dispersed in 30 mL of deionized water to get a homogeneous liquid mixture under the help of an ultrasonic cell disrupter. Then, 360 mg of $\text{Co}(\text{NO}_3)_2 \cdot 6\text{H}_2\text{O}$ ($\geq 98.0\%$, XiLong) and 50 mL 2-methylimidazole (2-mIM, $\geq 98.0\%$, Innochem) aqueous solution ($0.8 \text{ mol} \cdot \text{L}^{-1}$) was added to the above liquid mixture and continued stirring for 15 min. The precipitate of ZIF-67@CNT was filtrated, rinsed several times, and dried at 60°C overnight. Three sets of samples were prepared with varied CNT amounts of 5, 15, or 25 mg. Pure ZIF-67 was also obtained without CNTs.

2.1.2 Preparation of NiCoS (NCS/C) and NiCo-S@CNT (NCS/C/CNT)

First, 40 mg of ZIF-67 and ZIF-67@CNT precursors were respectively mixed with 100 mg of $\text{Ni}(\text{NO}_3)_2 \cdot 6\text{H}_2\text{O}$ ($\geq 98.0\%$, XiLong) and 80 mg thioacetamide (TAA, $\geq 99.0\%$, Sinopharm) in 30 mL ethanol. Subsequently, the mixture was heated at 120°C for 2 h in a 40 mL polytetrafluoroethylene autoclave. Then the solvothermal product was collected by centrifugation as well as rinsing with ethanol and deionized water. Finally, NCS/C and NCS/C/CNT were harvested over lyophilization for 24 h.

2.1.3 Preparation of P-NCS/C/CNT

The as-prepared product NCS/C/CNT and $\text{NaH}_2\text{PO}_4 \cdot \text{H}_2\text{O}$ ($\geq 98.0\%$, Innochem) were weighed at a mass ratio of 1:20 and put in separate ceramic boats in the same tube furnace, where the NCS/C/CNT boat was placed at the downstream and $\text{NaH}_2\text{PO}_4 \cdot \text{H}_2\text{O}$ boat was set at the upstream. Then, both boats were heated at $10^\circ\text{C} \cdot \text{min}^{-1}$ to 300°C for a maintenance of 60 min in Ar to obtain P-NCS@CNT.

2.2 Material characterization

X-ray powder diffraction (XRD) (D8 Advance 4000 V) with Cu $K\alpha$ radiation ($\lambda = 1.5418 \text{ \AA}$), ranging from 20° to 80° , was used to study the crystalline structure. To determine the morphology and microstructure, scanning electron microscopy (SEM), transmission electron microscopy (TEM), and corresponding energy dispersive spectroscopy (EDS) mapping were operated on Sirion200 (FEI) and H-8100 (Hitachi). X-ray photoelectron spectroscopy (XPS) was recorded by an X-ray photoelectron spectrometer (Escalab 250Xi) with monochromatic Al $K\alpha$ (1486.71 eV) and studied by a hemispherical electronic energy analyzer. The pore size distribution was measured by an automatic gas adsorption analyzer. The test of thermogravimetric analysis (TGA) was conducted under flowing air (PerkinElmer, Pyris 1).

2.3 Electrochemical measurements

Electrochemical tests were performed on the CHI760E electrochemical workstation under normal atmospheric and temperature. An Hg/HgO electrode and a Pt foil were used correspondingly as the reference electrode and counter electrode, which combined with a working electrode and an electrolyte of a $3 \text{ mol}\cdot\text{L}^{-1}$ KOH to form the three-electrode setup. The working electrode consisted of the active substance, polyvinylidene fluoride, and acetylene black (mass ratio of 8:1:1) on a nickel foam, with *N*-methyl-2-pyrrolidone (NMP) as solvent making a homogeneous slurry. The NMP solvent and absorbed water was removed by 60°C vacuum-drying for 24 h. At a potential range of 0–0.5 V, the galvanostatic charge–discharge (GCD) and the cyclic voltammetry (CV) measurements were performed with current densities of $1\text{--}20 \text{ A}\cdot\text{g}^{-1}$ and scan rates of $2\text{--}100 \text{ mV}\cdot\text{s}^{-1}$. The electrochemical impedance spectroscopy (EIS) measurements were recorded at 0.01 Hz–100 kHz under an alternate current with a potential amplitude of 5 mV. In a three-electrode system, the specific capacity (C , unit: $\text{C}\cdot\text{g}^{-1}$) of the test electrode was calculated by the equation of $C = \frac{It}{m}$, where I , t , and m represent the constant discharge current (unit: A), the discharge time (unit: s), and the active material loading mass (unit: g).

To prepare the asymmetric supercapacitor, the sample electrode, AC electrode, cellulose membrane, and $3 \text{ mol}\cdot\text{L}^{-1}$ KOH were employed as cathode, anode, separator, and electrolyte, respectively. The specific assembly processes were as follows: two strip nickel foams coated with the sample and AC respectively were placed opposite to each other, and a cellulose membrane was placed in the middle. Both ends of the nickel foams were wrapped with nickel wires as polar ear, which then were installed in thermoplastic tubes, injected with $3 \text{ mol}\cdot\text{L}^{-1}$ KOH, and heated for encapsulation to obtain flexible supercapacitors. The energy density (unit: $\text{W}\cdot\text{h}\cdot\text{kg}^{-1}$) and power density (unit: $\text{W}\cdot\text{kg}^{-1}$) were calculated by the formula of $E = \frac{0.5 \times C_d \times \Delta V}{3.6}$ and $P = \frac{3600 \times E}{\Delta t}$, where C_d , ΔV , and Δt represent the specific capacity (unit: $\text{C}\cdot\text{g}^{-1}$) of the device, the work voltage window (unit: V), and the discharge time (unit: s).

2.4 First-principle calculation

The behaviors of electrons of CoNi_2S_4 and P-doped CoNi_2S_4 (P- CoNi_2S_4) were studied in depth through first-principle by virtue of density functional theory (DFT). The simulation was performed using generalized gradient approximation, adopted the Perdew–Burke–Ernzerh. Monkhorst-pack grid of $11 \times 11 \times 15$ was selected for k point sampling in the first irreducible Brillouin zone, and the energy cutoff was set as 500 eV. The energy criteria for convergence of self-consistent optimization was set as

10^{-5} eV, and the optimized structural accuracy was set as -0.02 .

3 Results and discussion

3.1 First-principle calculations

According to DFT theory, the potential of CoNi_2S_4 and P-doped CoNi_2S_4 (P- CoNi_2S_4) in energy storage applications can be estimated by analysis of their intrinsic energy state and electronic structures, which was shown in Fig. 1. After geometry optimizing the crystal structures of CoNi_2S_4 and P- CoNi_2S_4 , the calculation of electronic structure was performed, as plotted in Figs. 1(a) and 1(b). Theoretically, after P doping in CoNi_2S_4 , the electronegativity of P atoms can realign the orbital electrons of Ni and Co atoms and as a result, leads to its band evolution. The band structure difference between CoNi_2S_4 (Fig. 1(c)) and P- CoNi_2S_4 (Fig. 1(d)) confirms this assumption. In P- CoNi_2S_4 , lower energy steps are rendered by the increased energy bands around the Fermi surface (located at 0 eV), which can render more effortless electron transfer from the valence band to the conduction band [33] and bring enhanced macroscopic conductivity in consequence. Moreover, from their total density of states (DOSs) in Fig. 1(e), the uninterrupted and strengthened electron states of P- CoNi_2S_4 near the Fermi level also validate that P doping can heighten the electronic conductivity of CoNi_2S_4 [34]. The projected DOS of Ni 3d is compared between CoNi_2S_4 and P- CoNi_2S_4 in Fig. 1(f). Obviously, P- CoNi_2S_4 has the more negative value of d band center, i.e., -2.0519 V, of the two samples, indicating that increasing electrons occupy around the Fermi surface after P doping, which is in favor of the naturally superior electrochemical activity of P- CoNi_2S_4 . Theoretically, the lower the D-band center is, the farther it is from the Fermi level, and the antibonding orbital after bonding of the adsorbent orbital is closer to the Fermi level. At the same time, the probability of filling the antibonding orbital with electrons increases, resulting in a decrease in the adsorption energy. In addition, low adsorption energy means rapid adsorption and desorption of ions, which is beneficial to improve the reactivity and achieve rapid charge and discharge. The above calculation results unfold a potential path to get the improved electrochemical activity of CoNi_2S_4 through P-doping.

3.2 Structure and morphology analysis

Figure 2 depicts the preparation flow chart of P-NCS@CNT using CNT-penetrated ZIF-67 (ZIF-67/CNT) as precursors [35]. Through ethanol-thermal treatment, the Co^{2+} in ZIF-67/CNT can be oxidized into Co^{3+} by the

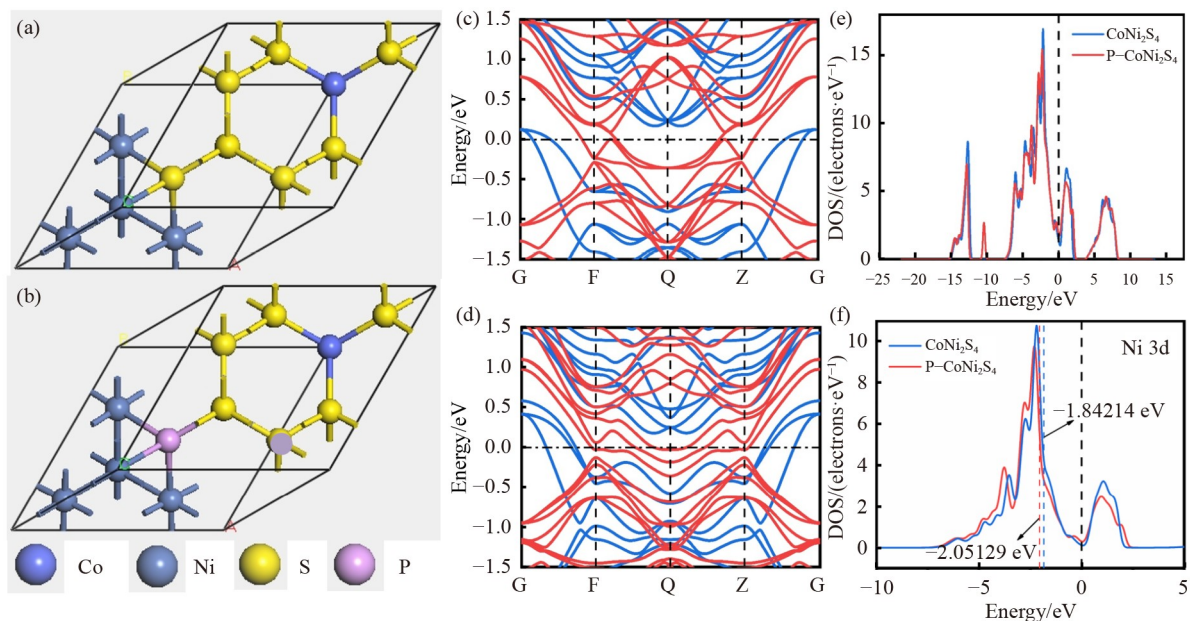


Fig. 1 Schematic diagram for the crystal structure of (a) CoNi_2S_4 and (b) $\text{P-CoNi}_2\text{S}_4$ after geometry optimization; calculated band structure of (c) CoNi_2S_4 and (d) $\text{P-CoNi}_2\text{S}_4$; (e) total DOSs for CoNi_2S_4 and $\text{P-CoNi}_2\text{S}_4$; (f) projected DOS of Ni 3d for CoNi_2S_4 and $\text{P-CoNi}_2\text{S}_4$.

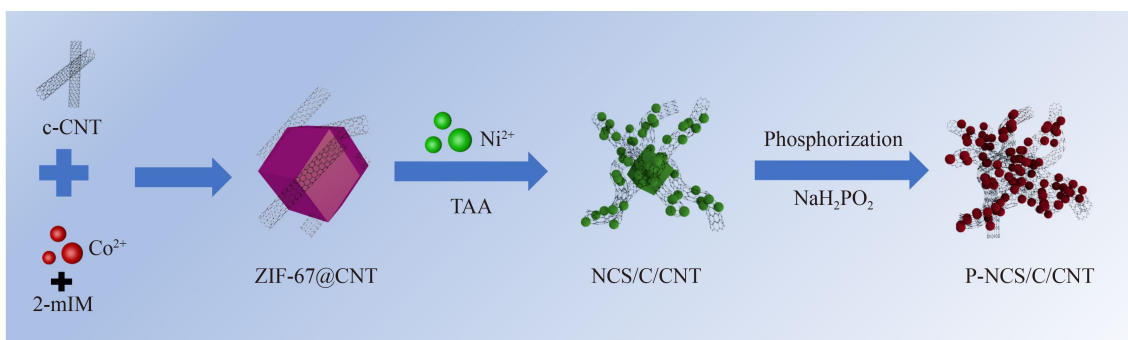


Fig. 2 Schematic illustration of the fabrication process of P-NCS/C/CNT.

Ni^{2+} from the hydrolysis of $\text{Ni}(\text{NO}_3)_2$. Meanwhile both metallic ions are co-precipitated by H_2S generated by the hydrolysis of TAA to form NCS [36]. Next, the above-prepared NCS/C/CNT is thermally annealed in the presence of a phosphorus source under flowing Ar to get P-NCS/C/CNT, which was proved in Fig. 3. Figure S1 (cf. Electronic Supplementary Material, ESM) proves the successful preparation of ZIF-67@CNT with its standard XRD pattern. The following product of NCS/C/CNT in Fig. 3(a) shows an XRD spectrum that refers to the coexistence phases of cubic CoNi_2S_4 (PDF#24-0334) and cubic NiS_2 (PDF# 80-0375), implying that NCSs have been prepared by the simple ethanol-thermal treatment. The characteristic peaks corresponded to the (311), (400), (511), and (440) crystal facet of CoNi_2S_4 , and the (200), (210), and (311) crystal facet of NiS_2 . Compared to the XRD pattern of pure NCS in Fig. S1(a), the additional characteristic peak at 26° in NCS/C/CNT is dominated by CNT (002) crystal plane. After the phosphidation reaction of NCS/C/CNT, the arisen distinct peaks from hexagonal

NiCoP (PDF#71-2336) indicate the successful P-doping. The characteristic peaks corresponded to the (111) and (201) crystal planes of NiCoP . It indicated that phosphorus has partially replaced the original sulfur in NCS/C/CNT. Simultaneously, new bonds with other elements can be formed when P substitutes for the S atom. Consequently, more active sites for the electrochemical reactions may be obtained, which is expected to achieve optimized electrochemical performance in P-NCS/C/CNT. Noting that some peaks are not found in NCS/C/CNT, which could be ascribed to the thermal treatment that helps to improve the crystallinity.

In their N_2 adsorption–desorption isotherms in Fig. S1(b), apparent hysteresis representing mesoporosity is found in NCS/C/CNT and P-NCS/C/CNT. While, in Fig. 3(b), the Barrett–Joyner–Halenda (BJH) curve of P-NCS/C/CNT shows numerous additional mesopores in the range of 2–5 nm compared to NCS/C/CNT. Besides, P-NCS/C/CNT rendered a higher BJH specific surface area of $56.765 \text{ m}^2\cdot\text{g}^{-1}$ than NCS@CNT ($16.937 \text{ m}^2\cdot\text{g}^{-1}$).

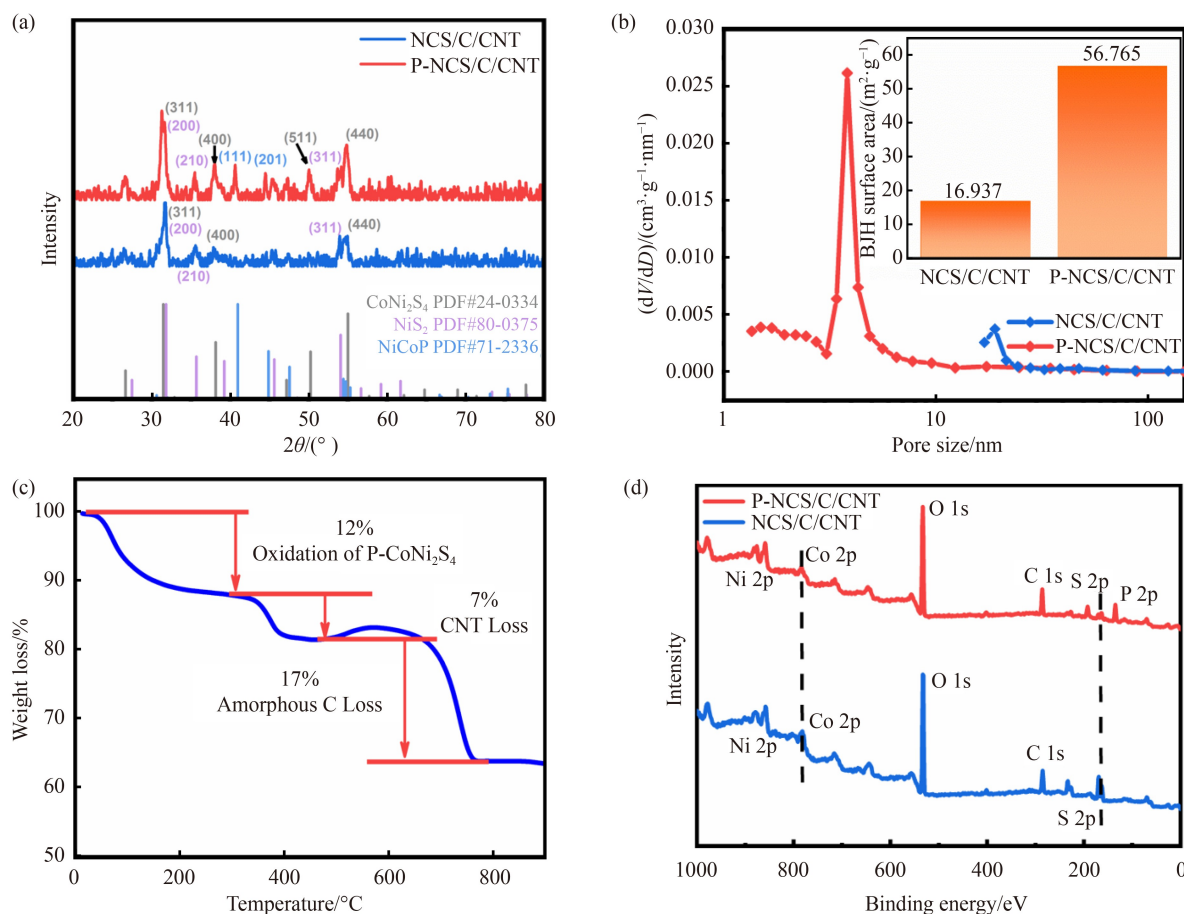


Fig. 3 (a) XRD patterns and (b) pore size distribution of NCS/C/CNT and P-NCS/C/CNT (the inset of (b) gives BJH surface areas); (c) TGA profile of P-NCS/C/CNT; (d) XPS survey spectra of NCS/C/CNT and P-NCS/C/CNT.

These facts verify the critical effect of phosphidation reaction in creating more mesopores and adding to larger specific surface areas, which are supposed to serve as activated sites for electrochemical reactions and matter exchange. To determine its component percentage, the TGA result of P-NCS/C/CNT in the air is analyzed in Fig. 3(c). The air oxidation of P-NCS contributed to the first mass loss from 50 to 300 °C. The followed mass loss happens from 300–450 and 600–750 °C due to the ignition loss of CNTs and amorphous carbon, respectively. Therefore, the overall carbon content in P-NCS/C/CNT is estimated to be 24%. The near-surface element composition of NCS/C/CNT and P-NCS/C/CNT is further verified in their XPS survey spectra (Fig. 3(d)). Apart from the common Ni, Co, S, O, and C peaks, the additional P peak of P-NCS/C/CNT identifies its composition with successful P doping.

From high-resolution XPS results (Fig. 4), the chemical states of the near-surface element can be studied in the two samples. Two sets of spin-orbit doublets occur in both high-resolution Co 2p spectra in Fig. 4(a), which refer to Co 2p_{3/2} and 2p_{1/2} separately. Each Co species contains double primary peaks and a shakeup satellite. Specifically, in Co 2p peaks of NCS/C/CNT, the peaks at

782.37 and 798.11 eV correspond to the Co²⁺ state as peaks at 778.43 and 793.35 eV are associated with the Co³⁺ state. It is believed that cobalt in ZIF-67 exists as Co(II) according to previously reported [37,38], therefore the Co²⁺ in ZIF-67/CNT was oxidized. Similarly, the binding energies at 857.13 and 875.18 eV are respectively characteristic of Ni 2p_{3/2} and 2p_{1/2} spin orbits of the Ni³⁺ state, while the binding energies at 853.16 and 870.60 eV refer to the Ni²⁺ state for Ni 2p spectrum of Fig. 4(b). For the S 2p spectrum of Fig. 4(c), the peaks at 160.96 and 162.28 eV, respectively correspond to S 2p_{3/2} and S 2p_{1/2} orbits of divalent sulfide ions (S²⁻) [39]. And the faint peaks assigned to the S₂²⁻ 2p_{3/2} and S₂²⁻ 2p_{1/2} at 164.20 and 165.31 eV reflects that there is S-rich structure in NCS/C/CNT and P-NCS/C/CNT. Moreover, the peak at 168.58 eV, triggered by sulfur oxide, is much weaker in P-NCS/C/CNT than NCS/C/CNT, implying that phosphorization facilitates the removal of some sulfur oxides induced by surface oxidation. Compared with NCS/C/CNT, P-NCS/C/CNT shows a slight negative peak shift to lower binding energy in all the 2p spectrums of Co, Ni, and S, probably caused by P atoms that influence the peripheral electrons of Co, Ni, and S. A charge redistribution may occur on the interfaces between NiCoP and

CoNi_2S_4 in the light of the deviations of bond energy [40]. As a consequence, the electrochemical performance of P-NCS/C/CNT can be improved. In addition, the C1s spectra (Fig. 4(d)) include three functional groups of C–C, C–O, and C=O with the binding energy of 284.37, 285.83, and 288.72 eV, respectively [41]. For the O 1s spectra (Fig. 4(e)), the metal–oxygen bonds, the absorbed oxygen, and C=O in CNT contribute to the peaks at 532.41, 533.39, and 531.04 eV, respectively [42]. For the P 2p spectrum of P-NCS/C/CNT (Fig. 4(f)), one can find two peaks at 128.90 and 129.90 eV referring to P $2p_{3/2}$ and $2p_{1/2}$, respectively, as well as a peak at 133.45 eV indexed as phosphate-like P [43].

SEM photos (Fig. 5) were taken to specify the morphology evolution during the synthesis of P-NCS/C/CNT. Original ZIF-67, as depicted in Fig. 5(a), renders typical rhomboid shape and rough surfaces, while the ZIF-67/CNT precursor in Fig. 5(b) shows that ZIF-67 with an average size of 200 nm penetrated and interconnected by CNTs. With the increase in CNT percentage, the overall morphology tends to be more uniform (Fig. S2, cf. ESM). Next, in Fig. 5(c), the NCS/C/CNT formed from ZIF-67/CNT shows tangled morphology with NCS/C lumps penetrated and interconnected with CNTs. In order to understand the effect of different amount of CNTs on the morphologies (Fig. S3, cf. ESM), it can be summarized

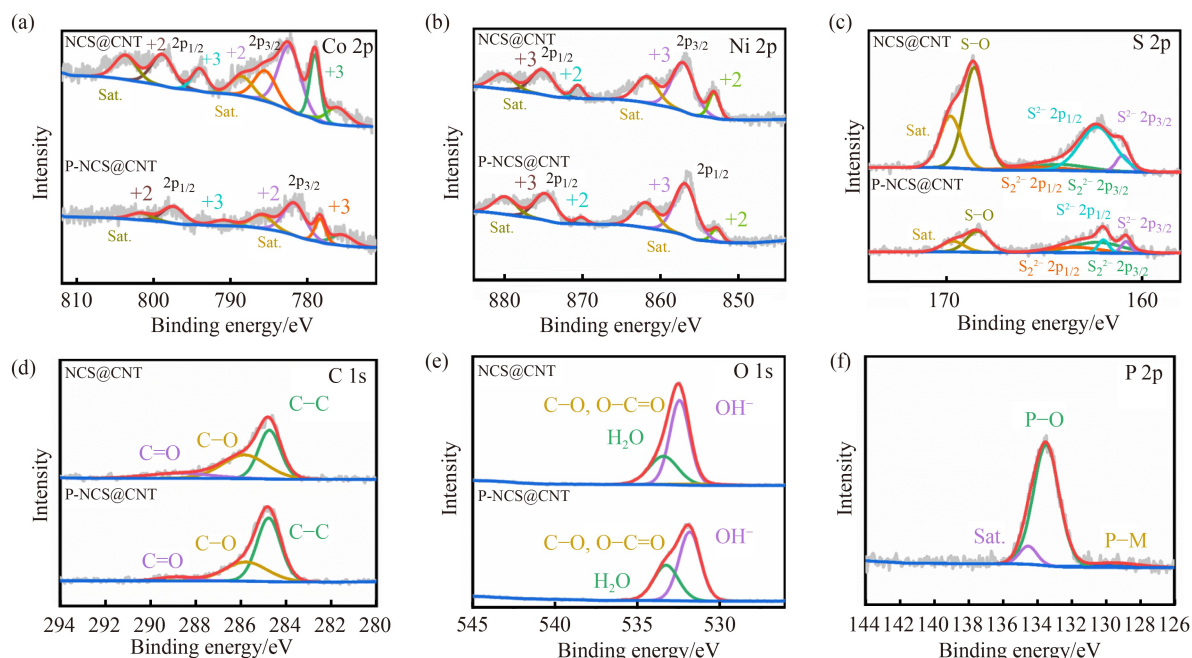


Fig. 4 XPS high-resolution spectra of (a) Co 2p, (b) Ni 2p, (c) S 2p, (d) C 1s, and (e) O 1s in NCS/C/CNT and P-NCS/C/CNT, and (f) P 2p in P-NCS/C/CNT.

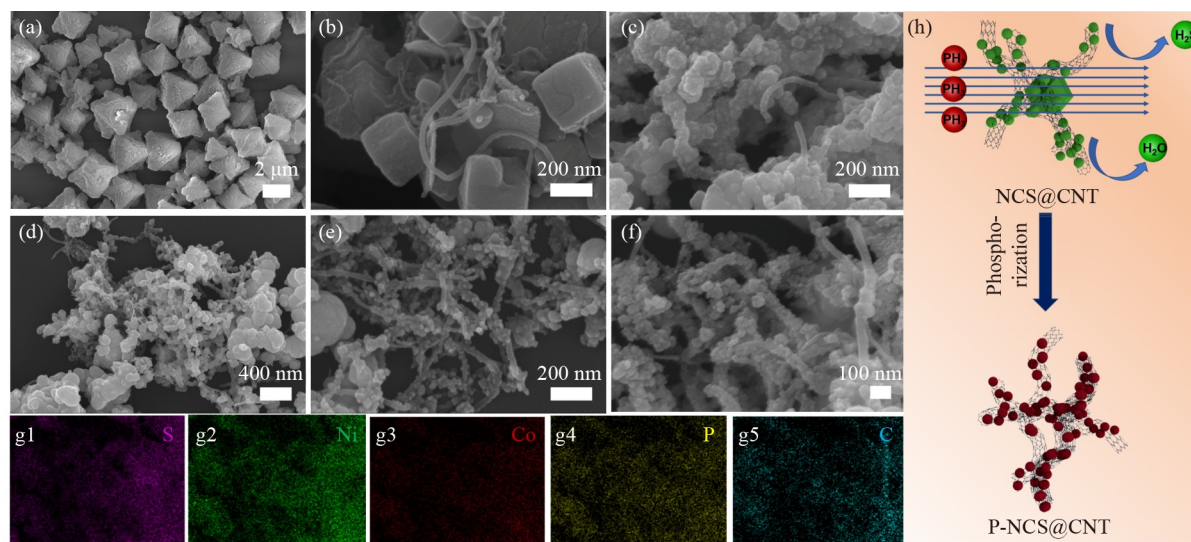


Fig. 5 SEM images of (a) ZIF-67, (b) ZIF-67@CNT, (c) NCS/C/CNT, and (d–f) P-NCS/C/CNT; SEM element maps of (g1) S, (g2) Ni, (g3) Co, (g4) P, and (g5) C in P-NCS/C/CNT; (h) the proposed mechanism before and after phosphorization.

by compare NCS/C, NCS/C/15CNT, and NCS/C/25CNT (Figs. S3(a–c)) that with the increased additive CNTs, a more dispersed structure is obtained, contributing to a more stable property. Finally, after phosphorization of NCS/C/CNT, the obtained lumps of Ni–Co compounds of P-NCS/C/CNT show apparent shrinkage in Figs. 5(d–f). The lump breakage and dispersed structure of Ni–Co compounds may be triggered by the particle fracture when S/O was substituted by P. Also, the PH_3 gas released by $\text{NaH}_2\text{PO}_2 \cdot \text{H}_2\text{O}$ further contributes to the elimination of $\text{H}_2\text{S}/\text{H}_2\text{O}$ (gas) from Ni/Co compounds (Fig. 5(h)), which adds to its more dispersed structure. Figure 5(g) shows distinct P profiles in P-NCS/C/CNT, consistent with the other elements of P, C, Ni, Co, and S, which, compared with the NCS@CNT in Fig. S3(d), confirms the uniform P doping in NCS.

To further uncover the morphology aspects of P-

NCS/C/CNT, TEM and high-resolution TEM (HRTEM) images were inspected (Fig. 6). Figures 6(a–c) shows the tangling structure between P-NCS and the CNTs penetrating through. By comparing CNTs in Fig. 6(c), it can be seen that the particle indicated was unique. Through the EDS maps, it can be judged that the particle material should be the prepared P-NCS rather than the original material from CNTs. The selective area electron diffraction (SAED) pattern of Fig. 6(d) proves the fact that the P-NCS are polycrystalline by distinguishable diffracting rings, among which the (220) crystallographic plane of NiCoP and the (311) plane of CoNi_2S_4 can be calibrated. From the HRTEM image of Fig. 6(e), two groups of crystal stripes can be found with lattice fringe distances of 2.72 Å and 2.15 Å, associated with the (222) facet of CoNi_2S_4 as well as the (110) facet of NiCoP, respectively. Fast Fourier transform (FFT) image is

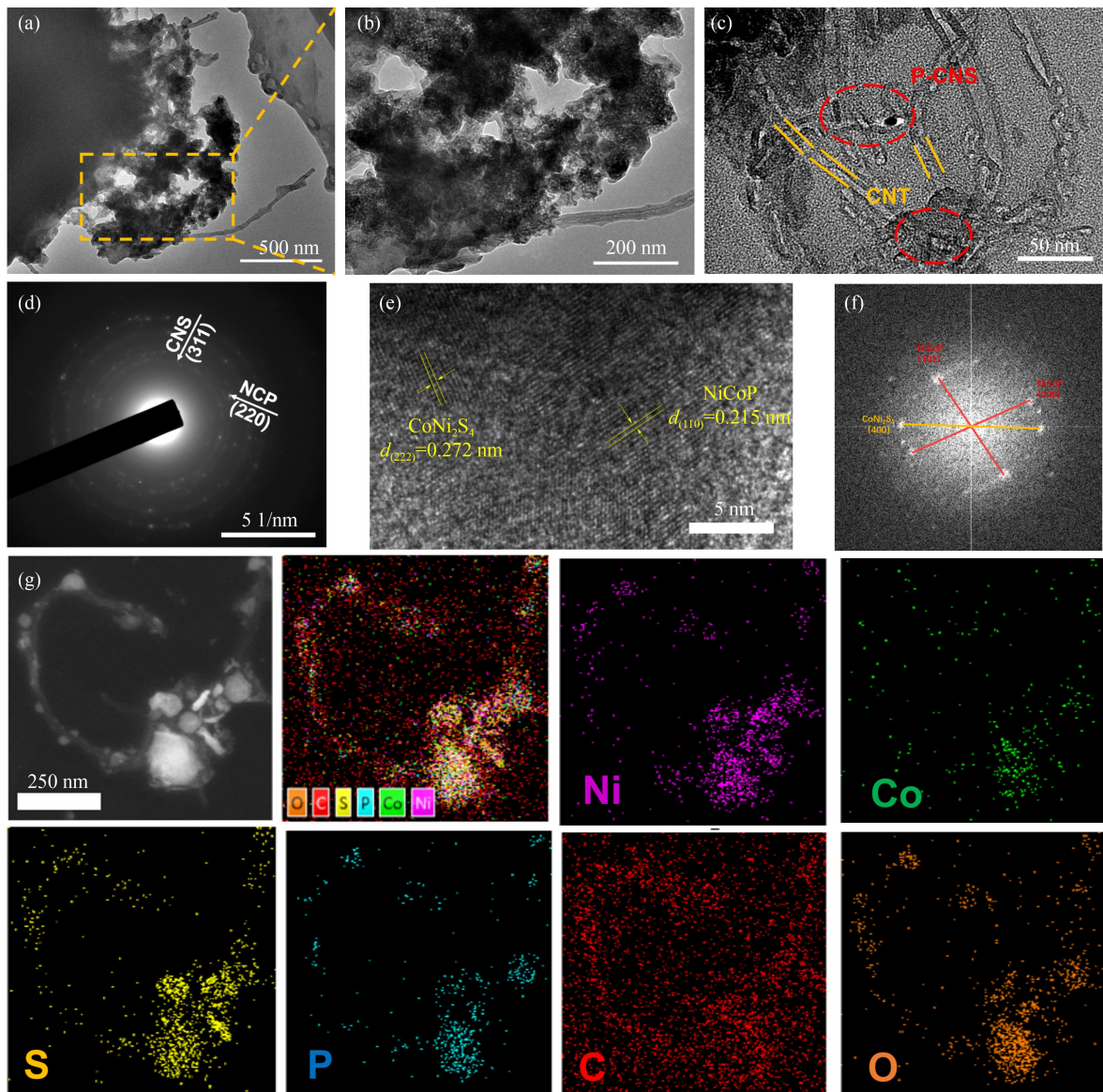


Fig. 6 (a–c) TEM images, (d) SAED patterns, (e) HRTEM images, (f) FFT image, and (g) EDS maps of P-NCS/C/CNT.

exhibited in Fig. 6(f), further verifying the crystal facet facts, in which the diffraction spots are indexed to the (400) facet of CoNi_2S_4 and the (101), (200) facet of NiCoP. The elemental spectrum (Fig. S4, cf. ESM) and mapping (Fig. 6(g)) of EDS demonstrate the element composition of Ni, Co, S, C, O, and P in P-NCS/C/CNT and confirm the uniform phosphorus doping, which also shown that the content of doped phosphorus was about 2.9 wt %.

3.3 Electrochemical properties

The electrochemical property of NCS/C, NCS/C/CNT, and P-NCS/C/CNT were tested and compared in a specific potential window to examine the impact of CNT adding and P-doped on the presented supercapacitive performance of NCS (Fig. 7). In Fig. 7(a), all CV curves at $10 \text{ mV}\cdot\text{s}^{-1}$ behave as integrated oxidation/reduction peaks in pairs consistent with the reversible Farady redox reactions of nickel (II/III) and cobalt (II/III) ions in alkaline electrolyte. Of three electrodes, P-NCS/C/CNT

owns the strongest current density response and the largest CV surrounding area, which indicates strengthened Farady reaction kinetics and superior charge storage due to CNTs and P doping. Next, by studying their GCD curves at $1 \text{ A}\cdot\text{g}^{-1}$ from Fig. 7(b), a non-linear feature with an evident voltage plateau around 0.25–0.31 V is rendered, marking the Farady, battery-like charge storage in NCS. Consistent with the CV results, P-NCS/C/CNT has a longer discharge duration time than the other two samples, implying its larger capacity. It is worth noting that optimized loading of CNT is the best solution considering both rate performance and capacity value. As shown in Figs. S5 and S6 (cf. ESM), investigating NCS/C/CNT in the CV and GCD curves at higher scanning rates and current densities, one can find that it outperformed others. The specific capacities of NCS/C with 5, 10, and 15 mg CNT shown the performance comparison result. It is obvious that when the loading mass was 5 mg, the composite exhibited the maximum specific capacity. Therefore, this value should be the optimal CNT content in the composite material.

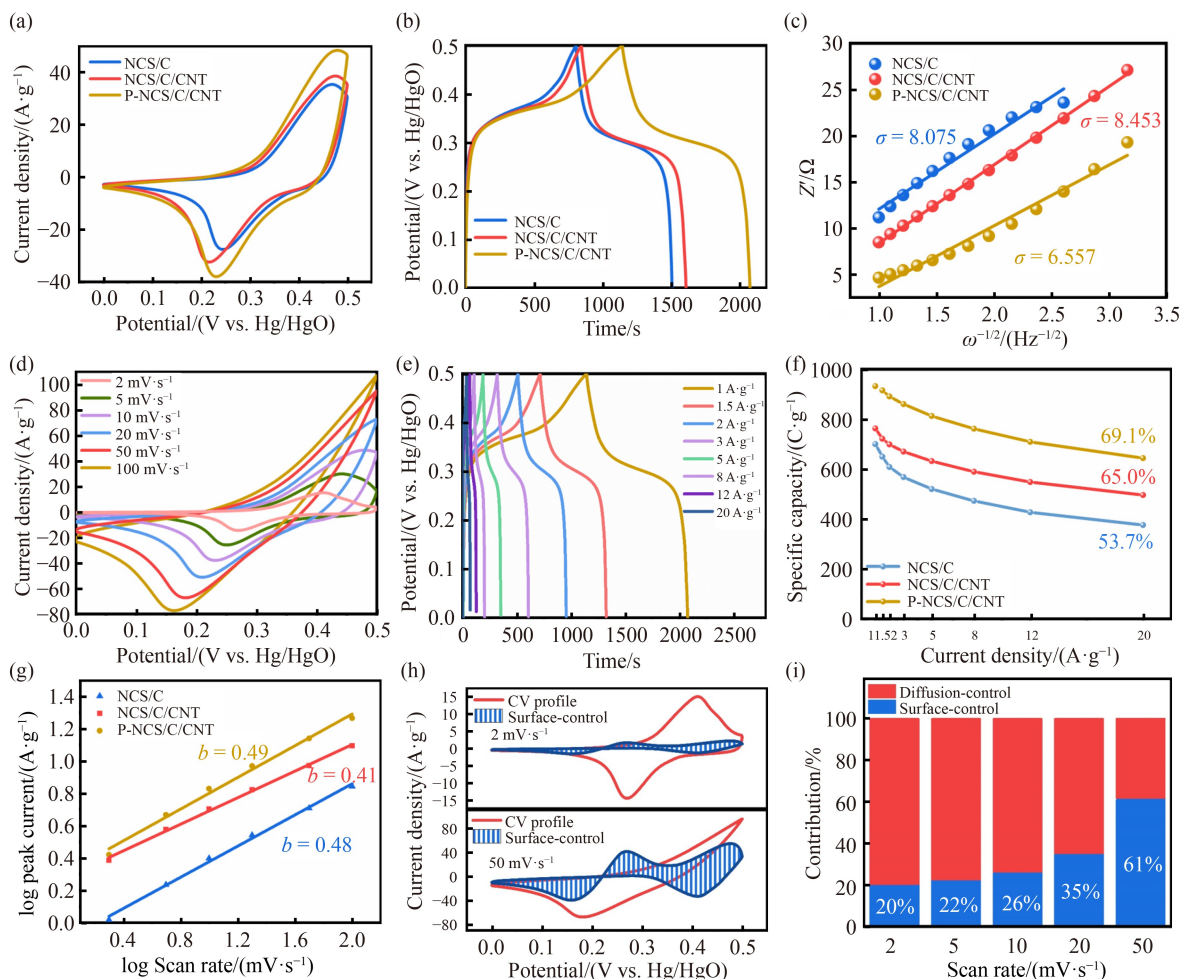


Fig. 7 (a) CV curves, (b) GCD curves, and (c) plots of Z' against $\omega^{-1/2}$ of NCS/C, NCS/C/CNT and P-NCS/C/CNT; (d) CV curves and (e) GCD curves of P-NCS/C/CNT; (f) specific capacity of NCS/C, NCS/C/CNT, and P-NCS/C/CNT; (g) the value of parameter b for NCS/C, NCS/C/CNT, and P-NCS/C/CNT; (h) typical CV profiles separating surface controlled contribution of NCS/C/CNT; and (i) summary of contribution ratios at different scan rates.

Figure S7 (cf. ESM) displays the EIS results of NCS/C, NCS/C/CNT, and P-NCS/C/CNT, which can be studied according to the equivalent circuit in its inset. A typical EIS curve can reflect the Warburg impedance (Z_W) representing ion diffusion at the electrolyte–electrode interface by the slope in the low-frequency zone, the charge transfer resistance by the semicircles at the higher frequency zone, and the bulk resistance (R_s) by the intercept points on the axis of the semicircles. On one hand, the R_s gradually decreases in the order of NCS/C, NCS/C/CNT, and P-NCS/C/CNT, presenting values of 0.665, 0.612, and 0.486 Ω , respectively. This indicates that the gradually reduced resistance by the incorporating of CNTs and P doping. On the other hand, all three samples show steep slopes at the low-frequency zone indicating the superiority of ZIF-67 derived NCS/C that owns sufficient inner porosity and renders superior ion diffusion ability. Figure 7(c) shows the $Z'-\omega^{-1/2}$ plots of all the samples, in which the diffusion coefficient is inversely proportional to the Warburg coefficient σ [19]. The σ obeys the equation of $Z' = R + \sigma\omega^{-1/2}$, where R and ω are the resistance and the angle frequency, respectively. Therefore, the slope of the $Z'-\omega^{-1/2}$ plot represents the σ . Gradually decreased σ are found in NCS/C, NCS/C/CNT, and P-NCS/C/CNT, which refers to increased ionic diffusion coefficient in order.

The CV and GCD curves of P-NCS/C/CNT are given in Figs. 7(d) and 7(e) detailedly. While the scanning rate increases, the CV curves of Fig. 7(d) basically maintain the same shape, each with a pair of clearly visible redox peaks, which illustrates its good reversibility and active ion transmission to fit with high scanning speed. The almost identical-shaped, symmetric GCD profiles of Fig. 7(e) further indicated the high reversibility and fast reaction kinetics of P-NCS/C/CNT. As summarized in Fig. 7(f), the P-NCS/C/CNT displays advantageous discharge capacity of 932.0, 914.7, 890.4, 860.1, 812.5, 761.6, 709.2, and 644.0 $C\cdot g^{-1}$ at 1, 1.5, 2, 3, 5, 8, 12, and 20 $A\cdot g^{-1}$, respectively, far beyond the values in NCS and NCS@CNT, which can only output capacity of 700.0 and 830.0 $C\cdot g^{-1}$ at 1 $A\cdot g^{-1}$. Concerning their capacity at 1 $A\cdot g^{-1}$, NCS/C, NCS/C/CNT, and P-NCS/C/CNT electrodes, respectively preserve about 53.7%, 65.0%, and 69.1% of the value when current densities increase to 20 $A\cdot g^{-1}$, showing orderly enhanced rate performance in NCS systems by CNT addition as well as P-doped. In addition, the supercapacitive performance in P-NCS/C/CNT is also higher than many other transition metal compound-based materials reported before (Table S1, cf. ESM).

Furthermore, the electrochemical impact of P doping on the energy storage process was worth exploring. To evaluate the capacity contribution of surface-controlled and diffusion-controlled processes in the charge/discharge half-cycles, the semiempirical equation of $i = av^b$ (a and b represent empirical parameters) was utilized based on the

CV technique in Fig. 7(d). In general, the b value close to 0.5 displays diffusion-controlled process via ion extraction/insertion, which close to 1 reveals surface-controlled process via ion adsorption/desorption. Figure 7(g) provides the $\log(i)-\log(v)$ plot whose slope gives the b value 0.48 for NCS/C, 0.41 for NCS/C/CNT and 0.49 for P-NCS/C/CNT. The value approaching 0.5 demonstrates the key role of the semi-infinite diffusion process. By distinguishing the proportion of surface-controlled current between diffusion-controlled current, the capacitive contributions were obtained [44] in Fig. 7(h), where the capacitive contributions of 20% and 61% are present at 2 and 100 $mV\cdot s^{-1}$, respectively. Moreover, the polarization of the electrode resulted in surface-controlled excessive capacitance contributions in some potential, which were reported previously [45,46]. The capacitive contributions varied from 2 to 100 $mV\cdot s^{-1}$ were summarized in Fig. 7(i). It is concluded that the diffusion-controlled capacity accounts for the majority of overall capacity, while the gradually enhanced capacitive contribution also plays a role in bringing higher high-rate capacity.

3.4 Electrochemical properties of the asymmetric supercapacitor

To test its value in practical applications (Figs. 8, S8, and S9, cf. ESM), P-NCS/C/CNT is combined with commercial AC to get a flexible asymmetric supercapacitor like Fig. 8(a). Unlike the battery-type P-NCS/C/CNT cathode, the CV and GCD curves of AC revealed in Figs. S8(a) and S8(b) anode demonstrates typical EDLC capacitance. As a result, the supercapacitor of P-NCS/C/CNT//AC displays reversible analogous rectangular-like CV curves in Figs. 8(b) and S8(c) due to the combining of the capacitive anode and pseudocapacitance P-NCS/C/CNT cathode. Obviously, in Fig. S8(c), the optimum potential window is 0–1.5 V which can bring steady CV curves with little polarization. At scanning rates varying in 2–100 $mV\cdot s^{-1}$, the CV curves present an almost similar shape with no polarization from Fig. 8(b). As for the CV curves of Fig. S9(a), of the overall current response, the capacitive contribution occupies about 16% at 2 $mV\cdot s^{-1}$ and 68% at 100 $mV\cdot s^{-1}$. As plotted in Fig. S9(b), the capacitive contribution of the supercapacitor from 5 to 50 $mV\cdot s^{-1}$ reveals the domination of the diffusion-limited process on charges stored reaction, and partly contributed by capacitive component at high scan rates, just like P-NCS/C/CNT. From the GCD curves of Fig. 8(c), the specific capacities of the supercapacitor were calculated as 167.4, 122.4, 105, 76.5, 57, and 44.1 $C\cdot g^{-1}$ at 0.5, 1, 1.5, 2, 3, and 4 $A\cdot g^{-1}$, respectively (Fig. 8(d)). Furthermore, according to the cycle examine in Fig. 8(e), the supercapacitor presents high stability by retaining 72.8% of the initial capacity till 3000 cycles at a high current density of 20 $A\cdot g^{-1}$. As for Fig. 8(f), the Ragone diagram reflects the energy density and power density level of the

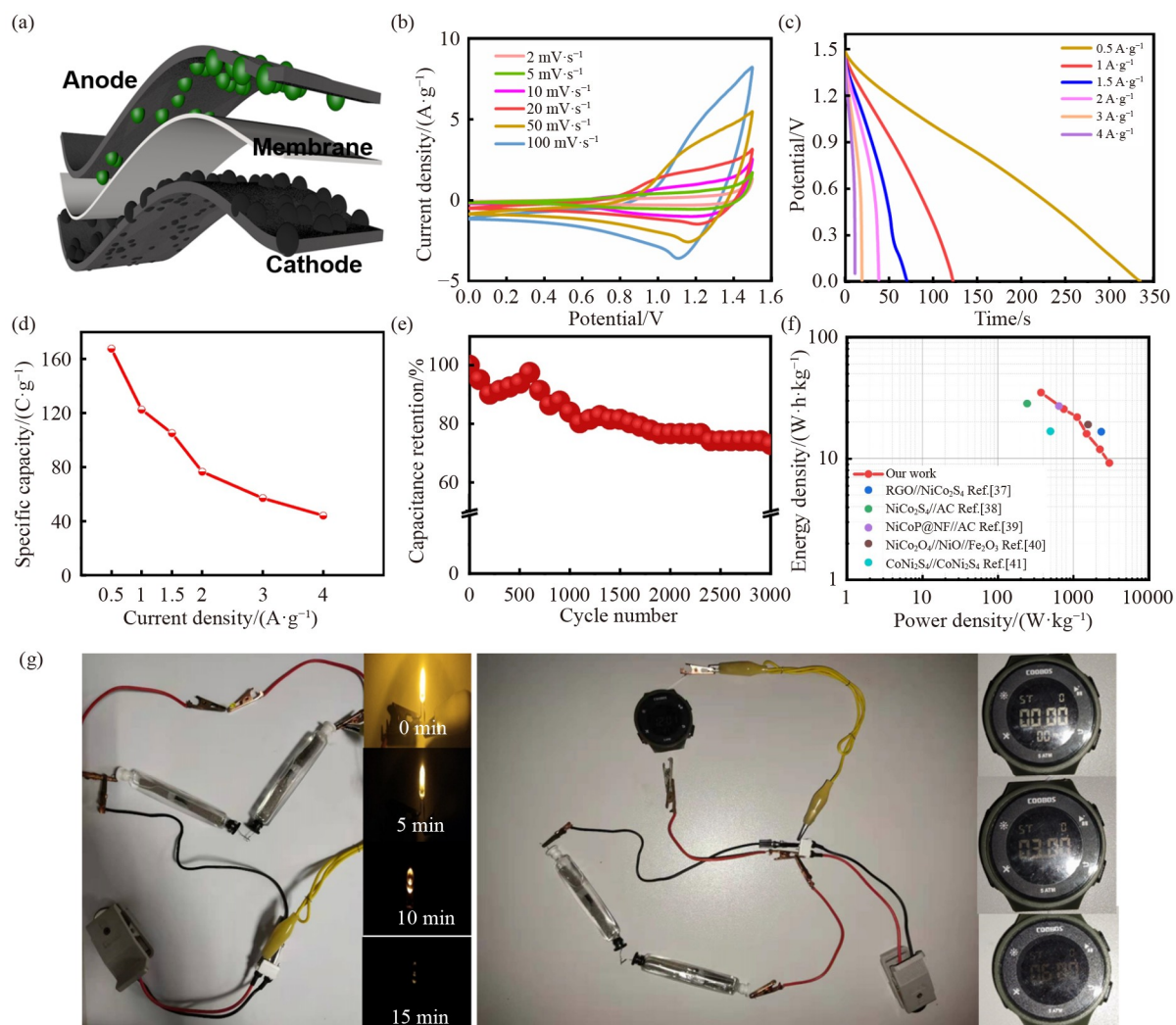


Fig. 8 Performance of the P-NCS/C/CNT//AC hybrid supercapacitor device: (a) schematic diagram, (b) CV curves, (c) GCD curves, (d) specific capacity, (e) capacity retention in long cycles, (f) Ragone plots, and (g) photos of the device driving an LED indicator and an electronic meter.

supercapacitor, which is equivalent to or better than other transition metal electrodes disclosed recently [47–51]. The largest energy density of $34.875 \text{ W}\cdot\text{h}\cdot\text{kg}^{-1}$ is reached when a power density is $375 \text{ W}\cdot\text{kg}^{-1}$, while the largest power density of $3000 \text{ W}\cdot\text{kg}^{-1}$ is reached when an energy density is $9.1875 \text{ W}\cdot\text{h}\cdot\text{kg}^{-1}$. Two such supercapacitors of P-NCS/C/CNT//AC in series can satisfy the voltage need of a yellow LED bulb or a digital watch. In Fig. 8(g), the yellow LED bulb can be lightened for up to fifteen minutes after only a one-minute charge. In Fig. 8(h), the digital watch can work for more than six minutes after a short charge. This verifies the practicability of this energy storage component.

The prominent electrochemical performances of the composite can be attributed to its design that renders the synergistic effect between P-NCS and C/CNT and favors direct electron and ion transport in the electrochemical process. First, the electronegativity of phosphorus helps to rearrange the electrons in Ni and Co orbitals, which

increases the active electrons and improves the conductivity. The optimization of the electronic structure by phosphorus doping promotes the electrochemical reactivity and improves the overall capacitive performance of the material. In addition, CNTs build the electron transport network as the bridge between P-NCS/C, realizing the electron transport in more directions. And CNTs as flexible materials can play a buffer role, improving the overall stability of the material. Since the double-layer capacitance provided by CNT is much smaller than that of pseudocapacitance, and its content in the composite was low, the capacity contributed by CNT could be negligible.

4 Conclusions

In summary, the potential of phosphorus doping to enhance the electrochemical performance of CoNi_2S_4 as a

supercapacitor electrode is uncovered through DFT. According to the first-principle calculation results, a novel bimetallic phosphosulfide of P-NCS/C is synthesized from the precursor of NCS/C utilizing a ZIF-67 template, which could result in superior electrochemical properties, indicating that the construction of NCS by phosphorus doping provides an available approach to strengthen faradaic pseudocapacitance performance. Meanwhile, a tiny amount of CNTs composited with P-NCS/C realized more dispersive synergetic microstructures of P-NCS/C/CNT. As for the resultant P-NCS/C/CNT composite, larger specific surface area and faster charge transportation were obtained by virtue of P-NCS/C entangled with CNTs. As a result, P-NCS/C/CNT exhibited high specific capacity, remarkable rate performance, and lower charge transfer resistance. Furthermore, a hybrid supercapacitor assembled with the P-NCS/C/CNT positive electrode could deliver a maximum power density of $3000 \text{ W}\cdot\text{kg}^{-1}$ at the energy density of $9.1875 \text{ W}\cdot\text{h}\cdot\text{kg}^{-1}$.

Acknowledgements This work was supported by the National Natural Science Foundation of China (Grant No. 522702045).

Electronic Supplementary Material Supplementary material is available in the online version of this article at <https://dx.doi.org/10.1007/s11705-022-2257-9> and is accessible for authorized users.

References

- Keum K, Kim J W, Hong S Y, Son J G, Lee S S, Ha J S. Flexible/stretchable supercapacitors with novel functionality for wearable electronics. *Advanced Materials*, 2020, 32(51): e2002180
- Ren K, Liu Z, Wei T, Fan Z. Recent developments of transition metal compounds-carbon hybrid electrodes for high energy/power supercapacitors. *Nano-Micro Letters*, 2021, 13(1): 129
- Jing C, Guo X, Xia L, Chen Y, Wang X, Liu X, Dong B, Dong F, Li S, Zhang Y. Morphologically confined hybridization of tiny CoNi_2S_4 nanosheets into S, P co-doped graphene leading to enhanced pseudocapacitance and rate capability. *Chemical Engineering Journal*, 2020, 379: 122305
- Xie J, Sun X, Zhang N, Xu K, Zhou M, Xie Y. Layer-by-layer β - $\text{Ni}(\text{OH})_2$ /graphene nanohybrids for ultraflexible all-solid-state thin-film supercapacitors with high electrochemical performance. *Nano Energy*, 2013, 2(1): 65
- Chodankar N R, Pham H D, Nanjundan A K, Fernando J F S, Jayaramulu K, Golberg D, Han Y K, Dubal D P. True meaning of pseudocapacitors and their performance metrics: asymmetric versus hybrid supercapacitors. *Small*, 2020, 16(37): e2002806
- Zhao Z, Xia K, Hou Y, Zhang Q, Ye Z, Lu J. Designing flexible, smart and self-sustainable supercapacitors for portable/wearable electronics: from conductive polymers. *Chemical Society Reviews*, 2021, 50(22): 12702
- Wang F, Wu X, Yuan X, Liu Z, Zhang Y, Fu L, Zhu Y, Zhou Q, Wu Y, Huang W. Latest advances in supercapacitors: from new electrode materials to novel device designs. *Chemical Society Reviews*, 2017, 46(22): 6816
- Wu L, Sun L, Li X, Zhang Q, Si H, Zhang Y, Wang K, Zhang Y. Mesoporous ZnCo_2O_4 -CNT microflowers as bifunctional material for supercapacitive and lithium energy storage. *Applied Surface Science*, 2020, 506: 144964
- Liu N, Pan Z, Ding X, Yang J, Xu G, Li L, Wang Q, Liu M, Zhang Y. *In-situ* growth of vertically aligned nickel cobalt sulfide nanowires on carbon nanotube fibers for high capacitance all-solid-state asymmetric fiber-supercapacitors. *Journal of Energy Chemistry*, 2020, 41: 209–215
- Liu Y, Li Z, Yao L, Chen S, Zhang P, Deng L. Confined growth of NiCo_2S_4 nanosheets on carbon flakes derived from eggplant with enhanced performance for asymmetric supercapacitors. *Chemical Engineering Journal*, 2019, 366: 550
- Yang Y, Zhang Y, Zhu C, Xie Y, Lv L, Chen W, He Y, Hu Z. Synthesis of ultrafine CoNi_2S_4 nanowire on carbon cloth as an efficient positive electrode material for high-performance hybrid supercapacitors. *Journal of Alloys and Compounds*, 2020, 823: 153885
- Hussain S, Hassan M, Javed M S, Shaheen A, Ahmad Shah S S, Nazir M T, Najam T, Khan A J, Zhang X, Liu G. Distinctive flower-like CoNi_2S_4 nanoneedle arrays (CNS-NAs) for superior supercapacitor electrode performances. *Ceramics International*, 2020, 46(16): 25942
- Dong J, Li S, Ding Y. Anchoring nickel-cobalt sulfide nanoparticles on carbon aerogel derived from waste watermelon rind for high-performance asymmetric supercapacitors. *Journal of Alloys and Compounds*, 2020, 845: 155701
- Gao X, Zhao Y, Dai K, Wang J, Zhang B, Shen X. NiCoP nanowire@NiCo-layered double hydroxides nanosheet heterostructure for flexible asymmetric supercapacitors. *Chemical Engineering Journal*, 2020, 384: 123373
- Zong Q, Yang H, Wang Q, Zhang Q, Zhu Y, Wang H, Shen Q. Three-dimensional coral-like $\text{NiCoP}@C@Ni(\text{OH})_2$ core-shell nanoarrays as battery-type electrodes to enhance cycle stability and energy density for hybrid supercapacitors. *Chemical Engineering Journal*, 2019, 361: 1
- Wan L, Wang Y, Zhang Y, Du C, Chen J, Xie M, Tian Z, Zhang W. Designing $\text{FeCoP}@NiCoP$ heterostructured nanosheets with superior electrochemical performance for hybrid supercapacitors. *Journal of Power Sources*, 2021, 506: 230096
- Wang M, Zhong J, Zhu Z, Gao A, Yi F, Ling J, Hao J, Shu D. Hollow NiCoP nanocubes derived from a Prussian blue analogue self-template for high-performance supercapacitors. *Journal of Alloys and Compounds*, 2022, 893: 162344
- Fan J, Wu K, Chen A, Wang M, Xie X, Fan J. Fingerprint-like NiCoP electrode material with rapid charging/discharging performance under large current density. *Journal of Alloys and Compounds*, 2022, 902: 163866
- Liu Y, Jiang G, Yu B, Evariste U, Ma P. Growth of phosphorus-substituted Ni–Co–S and iron oxide nanosheets on N-doped carbon nanofibers for high performance hybrid supercapacitor. *Journal of Alloys and Compounds*, 2020, 832: 154909
- Lin J, Wang Y, Zheng X, Liang H, Jia H, Qi J, Cao J, Tu J, Fei

- W, Feng J. P-doped NiCo₂S₄ nanotubes as battery-type electrodes for high-performance asymmetric supercapacitors. *Dalton Transactions*, 2018, 47(26): 8771
21. Jia H, Song Y, Wu J, Fu W, Zhao J, Liu X. A novel P-doped MnCo₂S₄ nanoneedles assembled dandelion-like structure for high performance hybrid supercapacitors. *Materials Letters*, 2018, 233: 55
 22. Xing T, Ouyang Y, Chen Y, Zheng L, Wu C, Wang X. P-doped ternary transition metal oxide as electrode material of asymmetric supercapacitor. *Journal of Energy Storage*, 2020, 28: 101248
 23. Chu W, Shi Z, Hou Y, Ma D, Bai X, Gao Y, Yang N. Trifunctional of phosphorus-doped NiCo₂O₄ nanowire materials for asymmetric supercapacitor, oxygen evolution reaction, and hydrogen evolution reaction. *ACS Applied Materials & Interfaces*, 2020, 12(2): 2763
 24. Zhao Y, Xue J, Chang J, Dai H. Amorphous phase induced high phosphorous-doping in dandelion-like cobalt sulfides for enhanced battery-supercapacitor hybrid device. *Journal of Electroanalytical Chemistry*, 2021, 889: 115231
 25. Wang Q, Qu Z, Chen S, Zhang D. Metal organic framework derived P-doping CoS@C with sulfide defect to boost high-performance asymmetric supercapacitors. *Journal of Colloid and Interface Science*, 2022, 624: 385–393
 26. Zhang J, Liu Y, Xia B, Sun C, Liu Y, Liu P, Gao D. Facile one-step synthesis of phosphorus-doped CoS₂ as efficient electrocatalyst for hydrogen evolution reaction. *Electrochimica Acta*, 2017, 259: 955–961
 27. Sun C, Sun L, Fan K, Shi Y, Ji G, Lin Y, Hu J, Zhang Y. A hollow Co₉S₈ rod-acidified CNT-NiCoLDH composite providing excellent electrochemical performance in asymmetric supercapacitors. *Dalton Transactions*, 2021, 50(26): 9283
 28. Shi Y, Sun L, Zhang Y, Si H, Sun C, Gu J, Gong Y, Li X, Zhang Y. SnS₂ nanodots decorated on RGO sheets with enhanced pseudocapacitive performance for asymmetric supercapacitors. *Journal of Alloys and Compounds*, 2021, 853: 156903
 29. Zhao W, Zheng Y, Cui L, Jia D, Wei D, Zheng R, Barrow C, Yang W, Liu J. MOF derived Ni–Co–S nanosheets on electrochemically activated carbon cloth via an etching/ion exchange method for wearable hybrid supercapacitors. *Chemical Engineering Journal*, 2019, 371: 461–469
 30. Sun J, Wu C, Sun X, Hu H, Zhi C, Li H, Yuan C. Recent progresses in high-energy-density all pseudocapacitive-electrode-materials-based asymmetric supercapacitors. *Journal of Materials Chemistry A: Materials for Energy and Sustainability*, 2017, 5(20): 9443–9464
 31. Hou L, Shi Y, Zhu S, Muhammad R, Pang G, Zhang X, Yuan C. Hollow mesoporous hetero-NiCo₂S₄/Co₉S₈ submicro-spindles: unusual formation and excellent pseudocapacitance towards hybrid supercapacitors. *Journal of Materials Chemistry A: Materials for Energy and Sustainability*, 2017, 5(1): 133–144
 32. Sun X, Sun J, Wu C, Guo L, Hou L, Yuan C. Unveiling composition/crystal structure-dependent electrochemical behaviors via experiments and first-principles calculations: rock-salt NiCoO₂ vs. spinel Ni_{1.5}Co_{1.5}O₄. *Materials Today. Energy*, 2021, 19: 100592
 33. Song L, Wang Q, Ye X, Yang F, Wang L, Wu Y, Xu F, Wang Y. Sulfide-fixed intrinsic porous NiCoP for boosting high capacitance and long-term stability. *ACS Materials Letters*, 2021, 3(7): 1016
 34. Gu J, Sun L, Zhang Y, Zhang Q, Li X, Si H, Shi Y, Sun C, Gong Y, Zhang Y. MOF-derived Ni-doped CoP@C grown on CNTs for high-performance supercapacitors. *Chemical Engineering Journal*, 2020, 385: 123454
 35. Guan B, Zhang Y, Fan L, Wu X, Wang M, Qiu Y, Zhang N, Sun K. Blocking polysulfide with Co₂B@CNT via “synergetic adsorptive effect” toward ultrahigh-rate capability and robust lithium-sulfur battery. *ACS Nano*, 2019, 13(6): 6742
 36. Yilmaz G, Yam K M, Zhang C, Fan H J, Ho G W. In situ transformation of MOFs into layered double hydroxide embedded metal sulfides for improved electrocatalytic and supercapacitive performance. *Advanced Materials*, 2017, 29(26): 1606814
 37. Wang Q, Gao F, Xu B, Ca F, Zhan F, Gao F, Wang Q. ZIF-67 derived amorphous CoNi₂S₄ nanocages with nanosheet arrays on the shell for a high-performance asymmetric supercapacitor. *Chemical Engineering Journal*, 2017, 327: 387–396
 38. Xia H, Zhang J, Yang Z, Guo S, Guo S, Xu Q. 2D MOF nanoflake-assembled spherical microstructures for enhanced supercapacitor and electrocatalysis performances. *Nano-Micro Letters*, 2017, 9(4): 43
 39. Gu H, Fan W, Liu T. Phosphorus-doped NiCo₂S₄ nanocrystals grown on electrospun carbon nanofibers as ultra-efficient electrocatalysts for the hydrogen evolution reaction. *Nanoscale Horizons*, 2017, 2(5): 277
 40. Ke G, Chen H, He J, Wu X C, Gao Y, Li Y, Mi H, Zhang Q, He C, Ren X. Ultrathin MoS₂ anchored on 3D carbon skeleton containing SnS quantum dots as a high-performance anode for advanced lithium ion batteries. *Chemical Engineering Journal*, 2021, 403: 126251
 41. Zhang Y, Sun L, Zhang L, Li X, Gu J, Si H, Wu L, Shi Y, Sun C, Zhang Y. Highly porous oxygen-doped NiCoP immobilized in reduced graphene oxide for supercapacitive energy storage. *Composites Part B: Engineering*, 2020, 182: 107611
 42. Liang H, Lin J, Jia H, Chen S, Qi J, Cao J, Lin T, Fei W, Feng J. Hierarchical NiCo-LDH/NiCoP@NiMn-LDH hybrid electrodes on carbon cloth for excellent supercapacitors. *Journal of Materials Chemistry A: Materials for Energy and Sustainability*, 2018, 6(31): 15040
 43. Sun C, Sun L, Zhang Y, Si H, Fan K, Shi Y, Gu J, Zhang Y. Reduced graphene oxide-modified NiCo-phosphates on Ni foam enabling high areal capacitances for asymmetric supercapacitors. *Journal of Materials Science and Technology*, 2021, 90: 255
 44. Yi M, Lu B, Zhang X, Tan Y, Zhu Z, Pan Z, Zhang J. Ionic liquid-assisted synthesis of nickel cobalt phosphide embedded in N, P codoped-carbon with hollow and folded structures for efficient hydrogen evolution reaction and supercapacitor. *Applied Catalysis B: Environmental*, 2021, 283: 119635
 45. Yang Y, Wang X, Huang F, Zhao J, Wang X. Ni(OH)₂ nanodot-decorated Co-Co LDH/C hollow nanocages for a high performance supercapacitor. *Dalton Transactions*, 2020, 49(47): 17310–17320
 46. Wang X, Huang F, Rong F, He P, Que R, Jiang S. Unique MOF-derived hierarchical MnO₂ nanotubes@NiCo-LDH/CoS₂

- nanocage materials as high performance supercapacitors. *Journal of Materials Chemistry A: Materials for Energy and Sustainability*, 2019, 7(19): 12018–12028
47. Zhu Y, Wu Z, Jing M, Yang X, Song W, Ji X. Mesoporous NiCo₂S₄ nanoparticles as high-performance electrode materials for supercapacitors. *Journal of Power Sources*, 2015, 273: 584
48. Chen H, Jiang J, Zhang L, Xia D, Yu Z, Guo D, Qi T, Wan H. In situ growth of NiCo₂S₄ nanotube arrays on Ni foam for supercapacitors: maximizing utilization efficiency at high mass loading to achieve ultrahigh areal pseudocapacitance. *Journal of Power Sources*, 2014, 254: 249
49. Lan Y, Zhao H, Zong Y, Li X, Sun Y, Feng J, Wang Y, Zheng X, Du Y. Phosphorization boosts the capacitance of mixed metal nanosheet arrays for high performance supercapacitor electrodes. *Nanoscale*, 2018, 10(25): 11775
50. Shanmugavani A, Selvan R K. Microwave assisted reflux synthesis of NiCo₂O₄/NiO composite: fabrication of high performance asymmetric supercapacitor with Fe₂O₃. *Electrochimica Acta*, 2016, 189: 283
51. Rajesh J A, Park J H, Vinh Quy V H, Kwon J M, Chae J Y, Kang S H, Kim H, Ahn K S. Rambutan-like cobalt nickel sulfide (CoNi₂S₄) hierarchitectre for high-performance symmetric aqueous supercapacitors. *Journal of Industrial and Engineering Chemistry*, 2018, 63: 73